INTERNATIONAL JOURNAL FOR NUMERICAL METHODS IN ENGINEERING
Int. J. Numer. Meth. Engng 2012; **89**:323–336
Published online 9 August 2011 in Wiley Online Library (wileyonlinelibrary.com). DOI: 10.1002/nme.3244

A computational procedure for prebending of wind turbine blades

Y. Bazilevs[1,*,†], M.-C. Hsu[1], J. Kiendl[2] and D. J. Benson[1]

[1]*Department of Structural Engineering, University of California, San Diego, 9500 Gilman Drive, La Jolla, CA 92093, U.S.A.*
[2]*Lehrstuhl für Statik, Technische Universität München, Arcisstrasse 21, 80333 München, Germany*

SUMMARY

Prebending of wind turbine blades constitutes a viable engineering solution to the problem of tower clearance, that is, ensuring that during wind turbine operation there is sufficient distance between the rotor blades and the tower to avoid collision. The prebent shape of the blade must be such that when the turbine rotor is subjected to wind and inertial loads, the blades are straightened into their design configuration. In this paper, we propose a method for accurate prediction of the prebent shape of wind turbine blades. The method relies on a stand-alone aerodynamics simulation that provides the wind loads on a rigidly spinning rotor, followed by a series of structural mechanics simulations to determine the stress-free prebent shape of the blade. This procedure involves only one-way coupling between the fluid and structural mechanics, which avoids the challenges of solving the coupled fluid–structure interaction problem. The proposed methodology, which has no limitations on the blade geometry and structural modeling, is successfully applied to prebending of a 63-m offshore wind turbine blade. Copyright © 2011 John Wiley & Sons, Ltd.

Received 7 December 2010; Revised 18 May 2011; Accepted 19 May 2011

KEY WORDS: wind turbine rotor; wind turbine blade; offshore wind; blade prebending; inverse deformation; computational fluid dynamics; computational structural mechanics; fluid–structure interaction; isogeometric analysis; composites; thin shells

1. INTRODUCTION

The rotor blades of a wind turbine need to be designed such that they do not strike the tower as the rotor turns in strong winds. There are several ways of avoiding this. One is to tilt the rotor so that the blades are not at a right angle to the nacelle. By the same token, it is possible to cone the rotor, thus ensuring tower clearance for the blades. However, both methods require adjustments to the nacelle design. As an alternative, blade prebending may be employed. In this case, the blades are manufactured to flex toward the wind when they are mounted on the tower and are not subjected to an inertial and wind loading. Once the blades are exposed to the wind, and the rotor starts turning, the blades are straightened to achieve their designed shape. This situation is graphically illustrated in Figure 1.

A typical reason for prebending of the wind turbine blades is to achieve ‘tower clearance’, that is, to make sure that there is sufficient distance between the blade tips and the tower during the wind turbine operation. Prebending of the blades engenders additional benefits. For example, the blades need not be quite as rigid because the amount of allowable deflection is greater. This makes it possible to use less material overall, and fewer processed materials, resulting in lighter and cheaper blades. Prebending of the blades also results in a more compact nacelle design. During operation, prebent

*Correspondence to: Y. Bazilevs, Department of Structural Engineering, University of California, San Diego, 9500 Gilman Drive, La Jolla, CA 92093, U.S.A.
†E-mail: yuri@ucsd.edu

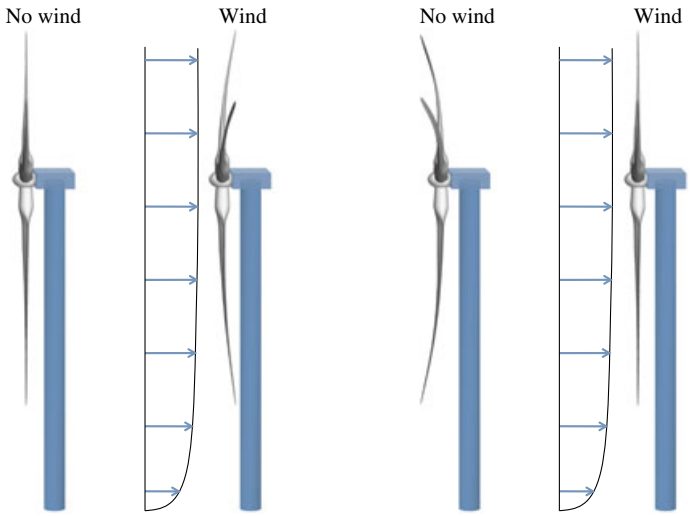

Figure 1. Using prebent blades to ensure tower clearance and rotor operation in its design configuration. (a) Without pre-bending and (b) with pre-bending.

blades straighten to their designed configuration, which is typically optimized for best possible aerodynamic performance.

Given the above advantages, it is important that one is able to determine the correct prebent shape given the blade structural and aerodynamic design and operating conditions. The latter involves wind and rotor speeds.

In this paper, we propose a methodology that makes use of standalone CFD and computational structural mechanics (CSM) procedures to obtain a prebent shape of the wind turbine blades. The main idea consists of performing a CFD simulation of a rigidly rotating rotor to obtain the aerodynamic load acting on the blade. Given the aerodynamic and inertial loads acting on the rotor design configuration, a stress-free prebent blade configuration is found using a simple iterative procedure that requires a sequence of CSM simulations. Note that in the proposed approach, the CFD and CSM procedures are decoupled, which avoids the challenges of solving coupled fluid–structure interaction problems.

However, the accuracy of the CFD and CSM procedures are essential for accurate prediction of the prebent blade shape. Our CFD simulation, which is 3D and time dependent (see Figure 2), is done using the method reported in [2]. The air flow is governed by the Navier–Stokes equations of incompressible flow in the ALE form. The residual-based variational multiscale turbulence modeling [4], in conjunction with isogeometric analysis based on nonuniform rational B-splines (NURBS) [5], are employed in the discretization of the fluid mechanics equations. The method was shown to give very good results for boundary-layer and rotating turbulent flows [2, 6–8], including the present application.

The wind turbine structural mechanics modeling makes use of the NURBS-based isogeometric rotation-free thin shell formulation [9], augmented with the bending strip method to handle more complex multipatch shell geometries [10]. The shell formulation is adapted for modeling of multilayer composite materials [3], which are employed in modern wind turbine blade designs.

The paper is outlined as follows. In Section 2, we formulate the nonlinear prebending problem and show its linearization. The linearized problem motivates an algorithm that essentially uses the displacement solution increments of the forward structural problem to march from the known current configuration to the unknown stress-free shape. In Section 3, we recall our thin shell structural mechanics formulation that is based on the Kirchhoff–Love theory, which neglects the through-thickness shearing deformations. To test whether this assumption remains valid for multilayer composites, we perform a comparison with a Reissner–Mindlin shell formulation that makes use of rotational DOFs. The numerical results indicate that the effect of the transverse shear is

DOI: 10.1002/nme

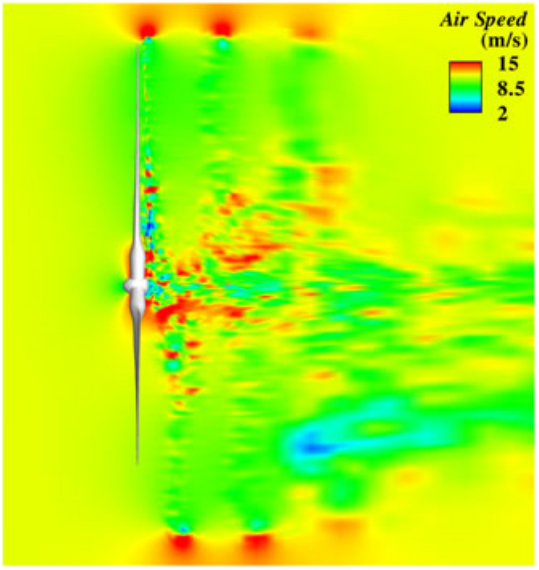

Figure 2. CFD simulation of a spinning rotor of a full-scale National Renewable Energy Laboratory (NREL) 5MW offshore baseline wind turbine. Isocontours of air speed on a planar cut. The rotor geometry was taken from [1] and converted into an isogeometric representation suitable for three-dimensional (3D) analysis. The results of 3D aerodynamics and fluid–structure interaction simulations of this rotor are presented in [2, 3].

negligible for the type of composite shells employed in the design of wind turbine blades. In Section 4, we present the numerical results of the prebending algorithm applied to a 63-m National Renewable Energy Laboratory (NREL) 5MW offshore baseline wind turbine blade [1] operating in realistic wind conditions. In Section 5, we draw our conclusions.

2. WIND TURBINE BLADE PREBENDING PROCEDURE

In this section, we formulate the blade prebending problem at the continuous level. The problem consists of finding the stress-free shape of the wind turbine blade, which, when loaded by the aerodynamic and inertial forces, assumes a known shape that is defined *a priori*. We also propose a simple algorithm to compute such a shape that makes use of a sequence of standard large-deformation structural problems.

2.1. Theory

We begin with the statement of virtual work: find the structural displacement $u_i \in (\mathcal{V}_0)_i$ such that for all virtual displacements $w_i \in (\mathcal{W}_0)_i$, $i = 1, \ldots, d$,

$$\int_{\Omega_0} \frac{\partial w_i}{\partial X_I} F_{iJ} S_{IJ} \mathrm{d}\Omega_0 = -\int_{\Omega} w_i \rho \frac{\partial^2 u_i}{\partial t^2}\Big|_X \mathrm{d}\Omega + \int_{\Omega} w_i \rho f_i \mathrm{d}\Omega + \int_{\Gamma^h} w_i t_i \mathrm{d}\Gamma, \tag{1}$$

where $d = 2, 3$ is the space dimension; $\Omega_0 \in \mathbb{R}^d$ is the unknown stress-free reference configuration; $(\mathcal{V}_0)_i$ and $(\mathcal{W}_0)_i$ are the function sets of Cartesian components of the admissible displacement vector and their variations, respectively, defined on the stress-free reference configuration; $\Omega \in \mathbb{R}^d$ is the known current or design configuration; $\boldsymbol{x}$ and $\boldsymbol{X}$ are the coordinates of the current and stress-free reference configurations, respectively; ρ is the density of the structure; f_i and t_i are the Cartesian components of the applied body force (e.g., gravity) and traction (e.g., aerodynamic stress) vector, respectively,

$$F_{iI} = \frac{\partial x_i}{\partial X_I} = I_{iI} + \frac{\partial u_i}{\partial X_I}, \tag{2}$$

DOI: 10.1002/nme

is the deformation gradient, S_{IJ} is the second Piola–Kirchhoff stress. Uppercase and lowercase indices are used to denote quantities in the reference and current configuration, respectively, and summation is employed on all repeated indices.

Although the virtual work equations hold true, the problem setup is unusual in that the stress-free reference configuration is unknown and the final configuration is given. To solve for the unknown reference configuration, we first transform the variational Equation (1) to the known current configuration as: find $u_i \in \mathcal{V}_i$, such that for all $w_i \in \mathcal{W}_i$

$$\int_\Omega \frac{\partial w_i}{\partial x_j}\sigma_{ij}\mathrm{d}\Omega = -\int_\Omega w_i \rho \frac{\partial^2 u_i}{\partial t^2}\Big|_X \mathrm{d}\Omega + \int_\Omega w_i \rho f_i \mathrm{d}\Omega + \int_{\Gamma^h} w_i t_i \mathrm{d}\Gamma, \tag{3}$$

where $\mathcal{V}_i$ and $\mathcal{W}_i$ are the current-configuration counterparts of $(\mathcal{V}_0)_i$ and $(\mathcal{W}_0)_i$, respectively, and σ_{ij}'s are the components of the Cauchy stress related to the second Piola–Kirchhoff stress by

$$\sigma_{ij} = F_{jI} F_{iJ} S_{IJ} J^{-1}. \tag{4}$$

We postpone the specification of the constitutive relationship until the next section. The developments in this section do not rely on a specific form of the constitutive law.

At this point we assume that the rotor spins around its axis at a constant angular speed and that the inflow wind conditions do not change. With this setup, the blade is subjected to a constant centripetal force and the aerodynamic load that may be averaged in time. The time average of the gravity load is zero for a body rotating around its center of mass. With these considerations, the time-averaged version of the variational Equation (3) may be written as: find $u_i \in \mathcal{V}_i$, such that for all $w_i \in \mathcal{W}_i$

$$\int_\Omega \frac{\partial w_i}{\partial x_j}\sigma_{ij}\mathrm{d}\Omega = -\int_\Omega w_i \rho [\boldsymbol{\omega} \times \boldsymbol{\omega} \times (\boldsymbol{x} - \boldsymbol{x}_0)]_i \mathrm{d}\Omega + \int_{\Gamma^h} w_i t_i \mathrm{d}\Gamma, \tag{5}$$

where the coordinate system of the current configuration is assumed to rotate with the blade, and $\boldsymbol{\omega}$ is a vector of angular velocities.

The variational problem (5) is nonlinear in the displacement u_i. A Newton–Raphson approach requires a linearization of (5), which we present in what follows. We first define an inverse of the deformation gradient

$$F^{-1}_{Ii} = \frac{\partial X_I}{\partial x_i} = I_{Ii} - \frac{\partial u_I}{\partial x_i}, \tag{6}$$

and note that, because the current configuration is known, F^{-1}_{Ii} is a *linear* function of the displacement vector u_I (which coincides with u_i component wise). The linearization of the stress terms in (5) may be computed as

$$\int_\Omega \frac{\partial w_i}{\partial x_j}\left(\frac{\partial \sigma_{ij}}{\partial F^{-1}_{Ik}}\right)\delta F_{Ik}\mathrm{d}\Omega = \int_\Omega \frac{\partial w_i}{\partial x_j}\left(\frac{\partial \sigma_{ij}}{\partial F^{-1}_{Ik}}\right)\left(-\frac{\partial \delta u_I}{\partial x_k}\right)\mathrm{d}\Omega, \tag{7}$$

where δu_I is the linearized displacement increment. Note that the rest of the terms in (5) are independent of the solution and may be computed once and for all. The partial derivative of the Cauchy stress with respect to the inverse of the deformation gradient in Equation (7) may be computed using the definition of the Cauchy stress given by Equation (4) and the standard identities from continuum mechanics (see, e.g., [11]). The details of the computation are presented in the appendix, while the end result is summarized here

$$\frac{\partial \sigma_{ij}}{\partial F^{-1}_{Ik}} = \left(-\sigma_{ij}F_{kI} + \sigma_{jk}F_{iI} + \sigma_{ki}F_{jI} + \overline{C}_{ijkl}F_{lI}\right), \tag{8}$$

DOI: 10.1002/nme

where $\overline{C}_{ijkl}$ is the push-forward of the material tensor C_{IJKL} to the current configuration, given by

$$\overline{C}_{ijkl} = C_{IJKL} F_{iI} F_{jJ} F_{kK} F_{lL} \det \mathbf{F}^{-1}. \tag{9}$$

Remark
The above formulation is precisely the inverse deformation problem, whose general formulation and treatment were proposed in [12] and further analyzed and studied computationally in [13]. In these references, the focus was placed on developing the right kinematic and stress measures for the inverse deformation problem. In this work, the emphasis is placed on the direct linearization of the inverse deformation equations, and the application to wind turbine blades.

Remark
The importance of the inverse deformation modeling was recently recognized in the area of fluid–structure interaction of arterial hemodynamics. Specifically, the scanned geometry of the blood vessel, which is subject to intramural blood pressure and viscous stress, may not be used as a stress-free reference configuration in the FSI computations of blood flow. Several computational methods to address this issue were proposed in [14–17].

The linearization given by Equation (7) may be used to solve the inverse deformation problem (5) using a standard Newton–Raphson procedure. Its implementation should not present too many difficulties. However, if, for whatever reason, the implementation is not possible, an alternative method for solving (5) may be desirable. In the following section we present an iterative approach to solving (5) that only makes use of the standard forward deformation problems.

2.2. Algorithm

We first note that in the case the stress-free reference and current configurations coincide, the linearized operator from Equation (7) becomes

$$\int_{\Omega} \frac{\partial w_i}{\partial x_j} C_{ijkl} \frac{\partial(-\delta u_k)}{\partial x_l} \mathrm{d}\Omega, \tag{10}$$

which is a linear elastic operator acting on the *negative* displacement increment. Hence, the linearization (7) suggests that at each nonlinear iteration a negative increment of the displacement or an increment of the displacement 'away from the current configuration' is found. This observation motivates the following algorithm for the computation of the stress-free reference configuration.

Initialization
Initialize the unknown reference configuration to coincide with the current configuration, that is,

$$\Omega_0 = \Omega, \tag{11}$$

which implies

$$\boldsymbol{u} = \mathbf{0}. \tag{12}$$

Step 1: Given the reference configuration Ω_0, a constitutive model, and prescribed boundary conditions, we solve the standard nonlinear structural problem: find the structural displacement $\boldsymbol{u}$ relative to Ω_0, such that for all $\boldsymbol{w}$,

$$\int_{\Omega_0} \frac{\partial w_i}{\partial X_I} F_{iJ} S_{IJ} \mathrm{d}\Omega_0 - F(\boldsymbol{w}) = 0, \tag{13}$$

where $F(\boldsymbol{w})$ is the right-hand side of Equation (5) given by

$$F(\boldsymbol{w}) = -\int_{\Omega} w_i \rho[\boldsymbol{\omega} \times \boldsymbol{\omega} \times (\boldsymbol{x} - \boldsymbol{x}_0)]_i \mathrm{d}\Omega + \int_{\Gamma^h} w_i t_i \mathrm{d}\Omega. \tag{14}$$

DOI: 10.1002/nme

The standard Newton–Raphson iteration is employed in this work to compute the solution of the nonlinear structural problem given by Equation (13).

Step 2: Given the displacement solution $\boldsymbol{u}$ from Step 1, update the reference configuration as

$$\Omega_0 = \{\boldsymbol{X} \mid \boldsymbol{X} = \boldsymbol{x} - \boldsymbol{u},\ \forall \boldsymbol{x} \in \Omega\}, \tag{15}$$

and return to Step 1 using $\boldsymbol{u}$ as the initial guess for the Newton–Raphson iteration.

Steps 1–2 are repeated until convergence, that is, until $\boldsymbol{u}$ satisfies Equation (13) and, as a consequence, Equation (5). In the sequel, we will illustrate the good performance of the proposed algorithm on a full-scale wind turbine blade subject to realistic wind and inertial loads.

3. STRUCTURAL MODELING OF WIND TURBINE BLADES

In this section, we briefly recall the structural modeling procedures that we employ to describe the behavior of the composite wind turbine blades. Because we rely on the Kirchhoff–Love rotation-free thin shell theory, we neglect the transverse shear effect, which may be important, especially in the presence of a multilayer composite material. We partially address this issue by comparing the Kirchhoff–Love and the Reissner–Mindlin shell results for the full-scale NREL 5MW offshore baseline wind turbine. The latter shell formulation makes use of both the displacement and rotational DOFs and is able to represent transverse shear effects (see, e.g., [18]).

3.1. Rotation-free thin shell formulation for wind turbine blade analysis

For the structural modeling of the wind turbine rotor blades, we use the bending strip method for rotation-free thin shell analysis. The bending strip method was first proposed and applied to elastostatic problems in [10] and further extended in [3] to consider dynamic phenomena and composite materials.

We define Γ_0^{s} and Γ^{s} to be the shell midsurface in the reference and deformed configuration, respectively. We assume that the shell structure is composed of N_{sp} surface patches, namely,

$$\Gamma_0^{\mathrm{s}} = \bigcup_{i=1}^{N_{\mathrm{sp}}} \Gamma_{0\,i}^{\mathrm{s}}, \tag{16}$$

$$\Gamma^{\mathrm{s}} = \bigcup_{i=1}^{N_{\mathrm{sp}}} \Gamma_i^{\mathrm{s}}, \tag{17}$$

where $\Gamma_{0\,i}^{\mathrm{s}}$ and Γ_i^{s}, $i = 1, 2, \ldots, N_{\mathrm{sp}}$, are the structural subdomains in the reference and deformed configuration, respectively. On the structural subdomain interiors we assume that the displacement field is described using C^1- or higher continuous basis functions. In this paper, we use NURBS to define the structural domain. The use of T-splines [19, 20], subdivision surfaces [21], or other smooth surface basis function technology is also possible. We insist that the surface patches are joined with at least C^0-continuity. In addition to the structural patches, we add N_{bp} bending strip patches

$$\Gamma_0^{\mathrm{b}} = \bigcup_{i=1}^{N_{\mathrm{bp}}} \Gamma_{0\,i}^{\mathrm{b}}, \tag{18}$$

whose role is to compensate for the lack of the necessary smoothness of the displacement field across the boundaries between the structural patches.

DOI: 10.1002/nme

With these definitions, we state the following variational formulation of the structure: find the shell midsurface displacement $\boldsymbol{u}$, such that for all $\boldsymbol{w}$

$$\begin{aligned}
&\int_{\Gamma_0^{\mathrm{s}}} \delta\boldsymbol{\varepsilon}(\boldsymbol{w}) : (\mathbf{A}(h)\boldsymbol{\varepsilon}(\boldsymbol{u}) + \mathbf{B}(h)\boldsymbol{\kappa}(\boldsymbol{u}))\,\mathrm{d}\Gamma_0^{\mathrm{s}} \; + \\
&\quad \int_{\Gamma_0^{\mathrm{s}}} \delta\boldsymbol{\kappa}(\boldsymbol{w}) : (\mathbf{B}(h)\boldsymbol{\varepsilon}(\boldsymbol{u}) + \mathbf{D}(h)\boldsymbol{\kappa}(\boldsymbol{u}))\,\mathrm{d}\Gamma_0^{\mathrm{s}} \; + \\
&\quad \int_{\Gamma_0^{\mathrm{b}}} \delta\boldsymbol{\kappa}(\boldsymbol{w}) : \frac{h^3}{12}\mathbf{C}^b\boldsymbol{\kappa}(\boldsymbol{u})\mathrm{d}\Gamma_0^{\mathrm{b}} \; + \\
&\quad \int_{\Gamma^{\mathrm{s}}} \boldsymbol{w}\cdot h\rho\boldsymbol{\omega}\times\boldsymbol{\omega}\times(\boldsymbol{x}-\boldsymbol{x}_0)\mathrm{d}\Gamma^{\mathrm{s}} - \int_{\Gamma^{\mathrm{s}}} \boldsymbol{w}\cdot\boldsymbol{t}\,\mathrm{d}\Gamma^{\mathrm{s}} = 0. \qquad (19)
\end{aligned}$$

In Equation (19), h is the local shell thickness, and $\boldsymbol{\varepsilon}$ and $\boldsymbol{\kappa}$ are the membrane strains and changes in curvature, respectively, which are suitable for large-deformation analysis (see [9] for details). Their variations, $\delta\boldsymbol{\varepsilon}(\boldsymbol{w})$ and $\delta\boldsymbol{\kappa}(\boldsymbol{w})$, are given by

$$\delta\boldsymbol{\varepsilon}(\boldsymbol{w}) = \lim_{\epsilon\to 0}\frac{\mathrm{d}}{\mathrm{d}\epsilon}\boldsymbol{\varepsilon}(\boldsymbol{u}+\epsilon\boldsymbol{w}), \qquad (20)$$

$$\delta\boldsymbol{\kappa}(\boldsymbol{w}) = \lim_{\epsilon\to 0}\frac{\mathrm{d}}{\mathrm{d}\epsilon}\boldsymbol{\kappa}(\boldsymbol{u}+\epsilon\boldsymbol{w}), \qquad (21)$$

where ϵ is a real number. It is assumed in Equation (19) that the linear stress–strain relationship for the structure holds (i.e., the St. Venant–Kirchhoff model). The structural formulation is objective and applicable to structures that undergo large deflections, while experiencing relatively low strains.

In Equation (19), $\mathbf{C}^{\mathrm{b}}$ is the constitutive material matrix for the bending strip patches. In the local Cartesian coordinate system oriented on the tangent vector orthogonal to the patch interface, $\mathbf{C}^{\mathrm{b}}$ may be expressed in Voigt notation as

$$\mathbf{C}^{\mathrm{b}} = \begin{bmatrix} E_s & 0 & 0 \\ 0 & 0 & 0 \\ 0 & 0 & 0 \end{bmatrix}, \qquad (22)$$

where E_s is the bending strip modulus of elasticity. The bending strip constitutive matrix is designed to ensure that no extra stiffness is added to the structure and that the bending moment is appropriately transferred between the structural patches. E_s scales linearly with the structural stiffness and, provided it is large enough, has little influence on the structural response [10]. As such, the bending strip method may be thought of as a physically-motivated penalty method.

In Equation (19), $\mathbf{A}(h)$, $\mathbf{B}(h)$, and $\mathbf{D}(h)$ are the extensional (membrane), coupling, and bending material stiffness tensors, respectively, given by

$$\mathbf{A}(h) = \frac{h}{n}\sum_{k=1}^{n}\overline{\mathbf{C}}_k, \qquad (23)$$

$$\mathbf{B}(h) = \frac{h^2}{n^2}\sum_{k=1}^{n}\overline{\mathbf{C}}_k\left(k-\frac{n}{2}-\frac{1}{2}\right), \qquad (24)$$

$$\mathbf{D}(h) = \frac{h^3}{n^3}\sum_{k=1}^{n}\overline{\mathbf{C}}_k\left[\left(k-\frac{n}{2}-\frac{1}{2}\right)^2+\frac{1}{12}\right], \qquad (25)$$

DOI: 10.1002/nme

where

$$\overline{\mathbf{C}}_k = \boldsymbol{T}^T(\phi_k)\,\mathbf{C}\,\boldsymbol{T}(\phi_k), \tag{26}$$

$$\mathbf{C} = \begin{bmatrix} \dfrac{E_1}{(1-\nu_{12}\nu_{21})} & \dfrac{\nu_{21}E_1}{(1-\nu_{12}\nu_{21})} & 0 \\ \dfrac{\nu_{12}E_2}{(1-\nu_{12}\nu_{21})} & \dfrac{E_2}{(1-\nu_{12}\nu_{21})} & 0 \\ 0 & 0 & G_{12} \end{bmatrix}, \tag{27}$$

$$\boldsymbol{T}(\phi) = \begin{bmatrix} \cos^2\phi & \sin^2\phi & \sin\phi\cos\phi \\ \sin^2\phi & \cos^2\phi & -\sin\phi\cos\phi \\ -2\sin\phi\cos\phi & 2\sin\phi\cos\phi & \cos^2\phi-\sin^2\phi \end{bmatrix}. \tag{28}$$

In the above equations, k denotes the k^{th} ply (or lamina), n be the total number of plies, and we assume that each ply has the same thickness h/n. ϕ is the fiber orientation angle in each ply, E_1 and E_2 are the Young's moduli of the unidirectional lamina, ν's are the Poisson's ratios, G_{12} is the shear modulus. The reader is referred to [3] for more details on the derivation of Equations (23)–(25).

3.2. Effect of the transverse shear

We perform elastostatic analysis of the NREL 5MW offshore baseline wind turbine blade (see [1] for the blade geometry definition) using the isogeometric Kirchhoff–Love shell analysis. We compare our results with an LS-DYNA [22] FEM simulation that makes use of a Reissner–Mindlin shell with rotational DOFs [18]. Note that in the latter case the transverse shear effect is taken into account. We consider two cases: isotropic and orthotropic material. For the isotropic case, the Young's modulus E and the Poisson's ratio ν are set to 19 GPa and 0.29, respectively. The anisotropic case corresponds to a symmetric fiberglass–epoxy composite with $[\pm 45/90/0_2]_s$ layup. The orthotropic elastic moduli for each ply are given in Table I. The entire blade is assumed to have the same layup. However, the variable blade thickness is considered from root to tip. The details of the blade thickness distribution are given in [3]. The blade aerodynamic loads are obtained from a separate CFD simulation, reported in [3], for which the wind speed is assumed uniform at 11.4 m/s, and the rotor speed is 1.267 rad/s.

Comparison of the tip deflection between the two shell formulations is shown in Table II. The difference in tip deflection is less than 1%. Figure 3 shows the overlapped deformed configuration obtained using the rotation-free formulation and that with rotational DOFs. Both deformed configurations are nearly indistinguishable. These results suggest that the use of a thin shell theory is suitable for this application, and that the transverse shear effect is not as important for accurate prediction of composite blade deformation under the action of wind and inertial (centripetal) loads.

Table I. Material properties of a unidirectional fiberglass–epoxy composite taken from [23].

E_1 (GPa)	E_2 (GPa)	G_{12} (GPa)	ν_{12} (–)	ρ (g/cm^3)
39	8.6	3.8	0.28	2.1

Table II. Comparison of the blade tip deflection between isogeometric Kirchhoff–Love (IGA-KL) and LS-DYNA Reissner–Mindlin shell analysis.

	Isotropic	Anisotropic
IGA-KL shell	3.48 m	3.73 m
LS-DYNA	3.51 m	3.76 m

DOI: 10.1002/nme

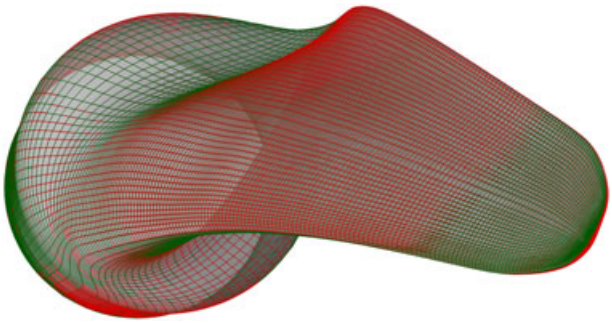

Figure 3. Comparison of the deformed blade shapes predicted by isogeometric Kirchhoff–Love (IGA-KL) and LS-DYNA Reissner–Mindlin shell analysis.

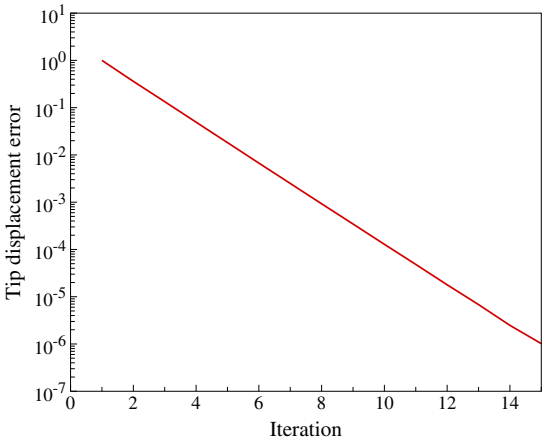

Figure 4. Blade tip displacement convergence as a function of the iteration number.

4. PREBENDING RESULTS OF THE NREL 5MW WIND TURBINE BLADE

A symmetric fiberglass–epoxy composite with $[\pm 45/0/90_2/0_3]_s$ layup, which enhances flap-wise and edge-wise stiffness, is considered for the rotor blade material. This layup presents a modification with respect to the blade design in the previous section. However, this layup is consistent with that reported in [3]. The choice of the layup in the previous section was made in order to facilitate the comparison with LS-DYNA calculations. The same wind conditions as in the previous section are assumed.

To arrive at a stress-free shape we employ the simplified algorithm from Section 2.2. Figure 4 shows the tip displacement convergence during the iterative process. After a few (five to six) iterations the tip exhibits no visible displacements, and the computation is stopped after a total of 15 iterations.

Figure 5 shows the initial and the final stress-free blade shapes. As expected, the blade bends into the wind and the tip deflection (from the current configuration) is predicted to be 5.61 m.

Next, we take a closer look at the stress distribution in the plies. For each ply we compute the Cauchy stress tensor components with respect to the local Cartesian basis that is aligned with the material axes. The first basis vector points in the direction of the fiber and the second in the direction of the matrix, which is orthogonal to the fiber direction. In Table III, we provide, $\sigma_1^{t,u}$ and $\sigma_1^{c,u}$, the longitudinal tensile and compressive strength, respectively, $\sigma_2^{t,u}$ and $\sigma_2^{c,u}$, the transverse tensile and compressive strength, respectively, and σ_{12}^{u}, the in-plane shear strength of the fiberglass–epoxy composite.

DOI: 10.1002/nme

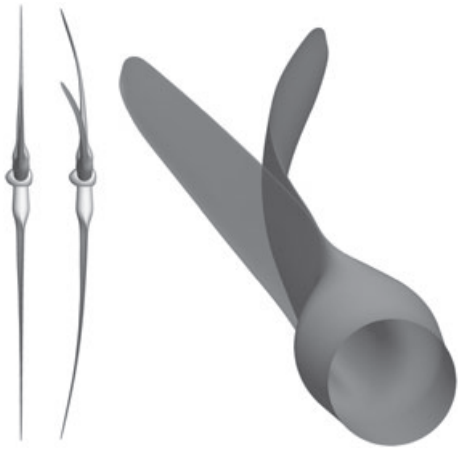

Figure 5. Left: rotor design configuration. Middle: rotor prebent configuration. Right: rotor blade design and prebent configurations superposed.

Table III. Strength of a unidirectional E-glass–epoxy composite lamina taken from [23].

$\sigma_1^{t,u}$ (MPa)	$\sigma_1^{c,u}$ (MPa)	$\sigma_2^{t,u}$ (MPa)	$\sigma_2^{c,u}$ (MPa)	σ_{12}^{u} (MPa)
1080	620	39	128	89

Table IV. Maximum lamina stresses normalized by the failure strength of a unidirectional E-glass–epoxy composite. The last column gives the Tsai–Wu failure criterion [24].

Ply no.	$\sigma_1^{t}/\sigma_1^{t,u}$	$\sigma_1^{c}/\sigma_1^{c,u}$	$\sigma_2^{t}/\sigma_2^{t,u}$	$\sigma_2^{c}/\sigma_2^{c,u}$	$\lvert\sigma_{12}\rvert/\sigma_{12}^{u}$	Tsai–Wu
16 (45°)	0.060	0.089	0.449	0.136	0.166	0.355
15 (−45°)	0.064	0.104	0.393	0.107	0.156	0.295
14 (0°)	0.042	0.107	0.586	0.136	0.055	0.516
13 (90°)	0.098	0.131	0.248	0.095	0.051	0.174
12 (90°)	0.097	0.132	0.208	0.078	0.047	0.141
11 (0°)	0.022	0.056	0.573	0.138	0.043	0.504
10 (0°)	0.016	0.039	0.569	0.138	0.042	0.500
9 (0°)	0.009	0.022	0.564	0.139	0.042	0.495
8 (0°)	0.010	0.018	0.560	0.139	0.043	0.491
7 (0°)	0.020	0.020	0.556	0.140	0.046	0.487
6 (0°)	0.030	0.031	0.552	0.140	0.048	0.484
5 (90°)	0.093	0.138	0.297	0.044	0.051	0.201
4 (90°)	0.092	0.139	0.357	0.052	0.056	0.255
3 (0°)	0.059	0.065	0.540	0.142	0.060	0.472
2 (−45°)	0.072	0.071	0.458	0.076	0.127	0.349
1 (45°)	0.069	0.066	0.528	0.089	0.133	0.419

The maximum values of the tensile σ^{t}, compressive σ^{c}, and in-plane shear stresses are computed for each ply and recorded in Table IV relative to the strength of the composite lamina. The highest ratio of the predicted Cauchy stress and the composite strength occurs for the tensile stress in the direction of the matrix material, that is, $\sigma_2^{t}/\sigma_2^{t,u}$. Although the ratio does not exceed 0.6, which means the predicted stress is below the composite failure strength, we feel this value is somewhat high. In the rest of the stress components the ratios are significantly lower. It is also evident from the table that the 0° plies are the most vulnerable in our design. The last column of Table IV also gives the Tsai–Wu failure criterion for every ply (see [24] for details). In this case, all the stress components are considered simultaneously, which gives a scalar-valued failure criterion that is widely used in practice.

DOI: 10.1002/nme

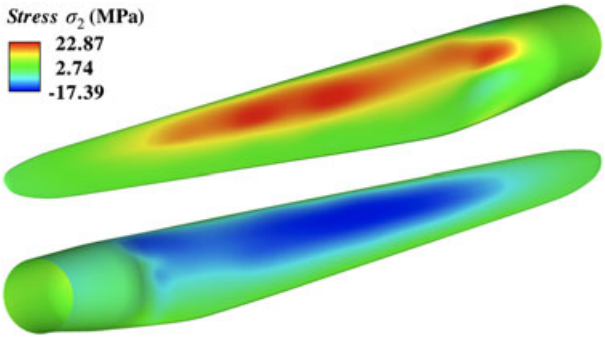

Figure 6. Normal stress distribution in the direction of the matrix material for the 0° ply number 14. Top: pressure side. Bottom: suction side.

Figure 6 shows the distribution of σ_2 in the 0° ply number 14, which has the highest ratio of $\sigma_2^{\mathrm{t}}/\sigma_2^{\mathrm{t},u}$ (see Table IV). The pressure side of the blade is in tension, while the suction side of the blade is in compression as expected. However, the level of the tensile stress is not very far from the tensile failure strength, which suggests that a stronger matrix material may be desirable for this blade design.

5. CONCLUSIONS

In this article, we proposed a method for wind turbine blade prebending. The method relies on stand-alone CFD and CSM computations, which makes it attractive from the standpoint of practical implementation. However, the accurate prediction of the prebent blade shape relies on the accuracy of the underlying CFD and SCM procedures. In this work, we made use of NURBS-based isogeometric analysis for both the fluid and structural modeling and simulation, and illustrated the good performance of the proposed prebending algorithm on a full-scale offshore wind turbine blade. In addition, we were able to show that the use of thin-shell approximation, which does not account for transverse shear effects, is well suited for wind turbine blades that are made of multilayer composite material.

APPENDIX A: DERIVATION OF THE LINEARIZED INVERSE MOTION PROBLEM

Focusing on the stress terms and starting from

$$\int_{\Omega_0} \frac{\partial w_i}{\partial X_I} F_{iJ} S_{IJ} \mathrm{d}\Omega_0, \tag{A.1}$$

we change variables to the known current configuration Ω

$$\int_{\Omega} \frac{\partial w_i}{\partial x_j} F_{jI} F_{iJ} S_{IJ} J^{-1} \mathrm{d}\Omega, \tag{A.2}$$

where $J = \det \mathbf{F}$. We take the variation of the above equation as

$$\begin{aligned} \delta \int_{\Omega} \frac{\partial w_i}{\partial x_j} F_{jI} F_{iJ} S_{IJ} J^{-1} \mathrm{d}\Omega &= \int_{\Omega} \frac{\partial w_i}{\partial x_j} \delta \left(F_{jI} F_{iJ} S_{IJ} J^{-1} \right) \mathrm{d}\Omega \\ &= \int_{\Omega} \frac{\partial w_i}{\partial x_j} S_{IJ} \delta \left(F_{jI} F_{iJ} J^{-1} \right) \mathrm{d}\Omega + \int_{\Omega} \frac{\partial w_i}{\partial x_j} F_{jI} F_{iJ} J^{-1} \delta S_{IJ} \mathrm{d}\Omega, \end{aligned} \tag{A.3}$$

where the last two terms on the second line may be thought of as the geometric and material contributions to the linearized problem, respectively.

DOI: 10.1002/nme

Geometric contribution

We define the deformation gradient and its inverse as

$$F_{iI} = \frac{\partial x_i}{\partial X_I} = I_{iI} + \frac{\partial u_i}{\partial X_I}, \tag{A.4}$$

$$F^{-1}_{Ii} = \frac{\partial X_I}{\partial x_i} = I_{Ii} - \frac{\partial u_I}{\partial x_i}. \tag{A.5}$$

We also make use of the following relationship:

$$\frac{\partial F_{iI}}{\partial F^{-1}_{Jj}} = -F_{iJ} F_{jI}, \tag{A.6}$$

which is a standard identity in continuum mechanics (see, e.g., [11]). Using these equations, we derive

$$\delta F_{jI} = \frac{\partial F_{jI}}{\partial F^{-1}_{Mk}} \delta F^{-1}_{Mk} = F_{jM} F_{kI} \frac{\partial \delta u_M}{\partial x_k}, \tag{A.7}$$

$$\delta \left(F_{jI} F_{iJ} \right) = \delta F_{jI} F_{iJ} + F_{jI} \delta F_{iJ} = \left(F_{jM} F_{kI} F_{iJ} + F_{jI} F_{iM} F_{kJ} \right) \frac{\partial \delta u_M}{\partial x_k}, \tag{A.8}$$

$$\delta J^{-1} = \frac{\partial J^{-1}}{\partial F^{-1}_{Mk}} \delta F^{-1}_{Mk} = -J^{-1} F_{kM} \frac{\partial \delta u_M}{\partial x_k}, \tag{A.9}$$

where δu_M is the displacement variation. This allows us to directly compute the geometric contribution to the linearized inverse motion problem

$$\begin{aligned}
&\int_\Omega \frac{\partial w_i}{\partial x_j} S_{IJ} \delta \left(F_{jI} F_{iJ} J^{-1} \right) \mathrm{d}\Omega \\
&\quad = \int_\Omega \frac{\partial w_i}{\partial x_j} \delta \left(F_{jI} F_{iJ} \right) S_{IJ} J^{-1} \mathrm{d}\Omega + \int_\Omega \frac{\partial w_i}{\partial x_j} F_{jI} F_{iJ} S_{IJ} \delta \left(J^{-1} \right) \mathrm{d}\Omega \\
&\quad = \int_\Omega \frac{\partial w_i}{\partial x_j} \left(F_{jM} F_{kI} F_{iJ} + F_{jI} F_{iM} F_{kJ} - F_{jI} F_{iJ} F_{kM} \right) S_{IJ} J^{-1} \frac{\partial \delta u_M}{\partial x_k} \mathrm{d}\Omega \\
&\quad = \int_\Omega \frac{\partial w_i}{\partial x_j} \left(-\sigma_{ij} F_{kM} + \sigma_{jk} F_{iM} + \sigma_{ki} F_{jM} \right) \frac{\partial \delta u_M}{\partial x_k} \mathrm{d}\Omega.
\end{aligned} \tag{A.10}$$

where we reintroduced the definition of the Cauchy stress $\sigma_{ij} = J^{-1} F_{iI} S_{IJ} F_{jJ}$.

Material contribution

We compute the following variations:

$$\begin{aligned}
\delta S_{IJ} &= \frac{\partial S_{IJ}}{\partial E_{KL}} \delta E_{KL} \equiv C_{IJKL} \delta E_{KL}, \\
\delta E_{KL} &= \frac{1}{2} \delta \left(F_{lK} F_{lL} - I_{KL} \right) \\
&= \frac{1}{2} \left(\delta F_{lK} F_{lL} + F_{lK} \delta F_{lL} \right) \\
&= \frac{1}{2} \left(\frac{\partial F_{lK}}{\partial F^{-1}_{Mk}} \delta F^{-1}_{Mk} F_{lL} + F_{lK} \frac{\partial F_{lL}}{\partial F^{-1}_{Mk}} \delta F^{-1}_{Mk} \right) \\
&= \frac{1}{2} \left(F_{lM} F_{kK} F_{lL} + F_{lK} F_{lM} F_{kL} \right) \frac{\partial \delta u_K}{\partial x_k}.
\end{aligned} \tag{A.11}$$

DOI: 10.1002/nme

Introducing these variations into the material contribution to the linearized inverse motion problem yields

$$\begin{aligned}
&\int_\Omega \frac{\partial w_i}{\partial x_j} F_{jI} F_{iJ} \delta(S_{IJ}) J^{-1} \mathrm{d}\Omega \\
&\quad = \int_\Omega \frac{\partial bc_i}{\partial x_j} F_{jI} F_{iJ} C_{IJKL} \frac{1}{2} (F_{kK} F_{lL} + F_{lK} F_{kL}) F_{lM} \frac{\partial \delta u_M}{\partial x_k} J^{-1} \mathrm{d}\Omega \\
&\quad = \int_\Omega \frac{\partial w_i}{\partial x_j} F_{iI} F_{jJ} C_{IJKL} F_{kK} F_{lL} F_{lM} \frac{\partial \delta u_M}{\partial x_k} J^{-1} \mathrm{d}\Omega, \qquad \text{(A.12)}
\end{aligned}$$

where the last equality is due to the minor symmetry of C_{IJKL}. We define

$$\overline{C}_{ijkl} \equiv F_{iI} F_{jJ} C_{IJKL} F_{kK} F_{lL} J^{-1}, \qquad \text{(A.13)}$$

and rewrite Equation (A.12) as

$$\int_\Omega \frac{\partial w_i}{\partial x_j} F_{jI} F_{iJ} \delta(S_{IJ}) J^{-1} \mathrm{d}\Omega = \int_\Omega \frac{\partial w_i}{\partial x_j} \overline{C}_{ijkl} F_{lM} \frac{\partial \delta u_M}{\partial x_k} \mathrm{d}\Omega. \qquad \text{(A.14)}$$

Combining the geometric and material terms, we arrive at the final result

$$\begin{aligned}
&\int_\Omega \frac{\partial w_i}{\partial x_j} \delta \left(F_{jI} F_{iJ} S_{IJ} J^{-1} \right) \mathrm{d}\Omega \\
&\quad = \int_\Omega \frac{\partial w_i}{\partial x_j} \left(-\sigma_{ij} F_{kM} + \sigma_{jk} F_{iM} + \sigma_{ki} F_{jM} + \overline{C}_{ijkl} F_{lM} \right) \frac{\partial \delta u_M}{\partial x_k} \mathrm{d}\Omega. \qquad \text{(A.15)}
\end{aligned}$$

ACKNOWLEDGEMENT

We thank the Texas Advanced Computing Center at The University of Texas at Austin for providing High Performance Computing (HPC) resources that have contributed to the research results reported within this paper. Y. Bazilevs and M.-C. Hsu were partially supported by the Los Alamos – UC San Diego Educational Collaboration Fellowship. Y. Bazilevs would also like to acknowledge the support of the NSF CAREER Award and the Hellman Fellowship. J. Kiendl was funded by the International Graduate School of Science and Engineering at the Technische Universität München.

REFERENCES

1. Jonkman J, Butterfield S, Musial W, Scott G. Definition of a 5-MW reference wind turbine for offshore system development. *NREL/TP-500-38060*, National Renewable Energy Laboratory, Golden, CO, 2009.
2. Bazilevs Y, Hsu M-C, Akkerman I, Wright S, Takizawa K, Henicke B, Spielman T, Tezduyar T. E. 3D simulation of wind turbine rotors at full scale. Part I: geometry modeling and aerodynamics. *International Journal for Numerical Methods in Fluids* 2011; **65**:207–235.
3. Bazilevs Y, Hsu M-C, Kiendl J, Wüchner R, Bletzinger K-U. 3D simulation of wind turbine rotors at full scale. Part II: fluid–structure interaction modeling with composite blades. *International Journal for Numerical Methods in Fluids* 2011; **65**:236–253.
4. Bazilevs Y, Calo VM, Cottrel JA, Hughes TJR, Reali A, Scovazzi G. Variational multiscale residual-based turbulence modeling for large eddy simulation of incompressible flows. *Computer Methods in Applied Mechanics and Engineering* 2007; **197**:173–201.
5. Hughes TJR, Cottrell JA, Bazilevs Y. Isogeometric analysis: CAD, finite elements, NURBS, exact geometry and mesh refinement. *Computer Methods in Applied Mechanics and Engineering* 2005; **194**:4135–4195.
6. Bazilevs Y, Akkerman I. Large eddy simulation of turbulent Taylor–Couette flow using isogeometric analysis and the residual–based variational multiscale method. *Journal of Computational Physics* 2010; **229**:3402–3414.
7. Bazilevs Y, Michler C, Calo VM, Hughes TJR. Weak Dirichlet boundary conditions for wall-bounded turbulent flows. *Computer Methods in Applied Mechanics and Engineering* 2007; **196**:4853–4862.
8. Bazilevs Y, Michler C, Calo VM, Hughes TJR. Isogeometric variational multiscale modeling of wall-bounded turbulent flows with weakly-enforced boundary conditions on unstretched meshes. *Computer Methods in Applied Mechanics and Engineering* 2010; **199**:780–790.
9. Kiendl J, Bletzinger K-U, Linhard J, Wüchner R. Isogeometric shell analysis with Kirchhoff–Love elements. *Computer Methods in Applied Mechanics and Engineering* 2009; **198**:3902–3914.

DOI: 10.1002/nme

10. Kiendl J, Bazilevs Y, Hsu M-C, Wüchner R, Bletzinger K-U. The bending strip method for isogeometric analysis of Kirchhoff–Love shell structures comprised of multiple patches. *Computer Methods in Applied Mechanics and Engineering* 2010; **199**:2403–2416.
11. Holzapfel GA. *Nonlinear solid mechanics, a continuum approach for engineering*. Wiley: Chichester, 2000.
12. Shield RT. Inverse deformation results in finite elasticity. *ZAMP* 1967; **18**:381–389.
13. Govindjee S, Mihalic PA. Computational methods for inverse finite elastostatics. *Computer Methods in Applied Mechanics and Engineering* 1996; **136**:47–57.
14. Bazilevs Y, Hsu M-C, Zhang Y, Wang W, Kvamsdal T, Hentschel S, Isaksen J. Computational fluid–structure interaction: methods and application to cerebral aneurysms. *Biomechanics and Modeling in Mechanobiology* 2010; **9**:481–498.
15. Hsu M-C, Bazilevs Y. Blood vessel tissue prestress modeling for vascular fluid–structure interaction simulation. *Finite Elements in Analysis and Design* 2011; **47**:593–599.
16. Takizawa K, Christopher J, Tezduyar TE, Sathe S. Space–time finite element computation of arterial fluid–structure interactions with patient-specific data. *Communications in Numerical Methods in Engineering* 2010; **26**:101–116.
17. Tezduyar TE, Sathe S, Schwaab M, Conklin BS. Arterial fluid mechanics modeling with the stabilized space–time fluid–structure interaction technique. *International Journal for Numerical Methods in Fluids* 2008; **57**:601–629.
18. Benson DJ, Bazilevs Y, Hsu MC, Hughes TJR. Isogeometric shell analysis: the Reissner–Mindlin shell. *Computer Methods in Applied Mechanics and Engineering* 2010; **199**:276–289.
19. Bazilevs Y, Calo VM, Cottrell JA, Evans JA, Hughes TJR, Lipton S, Scott MA, Sederberg TW. Isogeometric analysis using T-splines. *Computer Methods in Applied Mechanics and Engineering* 2010; **199**:264–275.
20. Dörfel MR, Jüttler B, Simeon B. Adaptive isogeometric analysis by local *h*-refinement with T-splines. *Computer Methods in Applied Mechanics and Engineering* 2010; **199**:264–275.
21. Cirak F, Ortiz M, Schröder P. Subdivision surfaces: a new paradigm for thin shell analysis. *International Journal for Numerical Methods in Engineering* 2000; **47**:2039–2072.
22. LS-DYNA Finite Element Software, Livermore Software Technology Corporation (LSTC), Livermore, California, USA. www.lstc.com/lsdyna.htm.
23. Daniel IM, Ishai O. *Engineering mechanics of composite materials*. Oxford University Press: New York, NY, 1994.
24. Tsai SW, Wu EM. A general theory of strength for anisotropic materials. *Journal of Composite Materials* 1971; **5**:58–80.

DOI: 10.1002/nme